Structural effects of LaNiO$_3$ as electrocatalyst for the oxygen reduction reaction

María Retuerto [a],*, Amaru González Pereira [a], Francisco J. Pérez-Alonso [a], Miguel A. Peña [a], José Luis G. Fierro [a], José Antonio Alonso [b], María Teresa Fernández-Díaz [c], Laura Pascual [a], Sergio Rojas [a],*

[a] Instituto de Catálisis y Petroleoquímica CSIC. C/Marie Curie 2, 28049, Madrid, Spain
[b] Instituto de Ciencia de Materiales de Madrid, CSIC. C/Sor Juana Inés de la Cruz 3, 28049 Madrid, Spain
[c] Institut Laue-Langevin, BP156X, Grenoble, F-38042, France

ABSTRACT

LaNiO$_3$ perovskite is a promising electrocatalyst for the oxygen reduction reaction (ORR). In this work we study the effects of several key structural and morphological features on the performance of LaNiO$_3$ perovskites for the ORR. We have prepared a series of LaNiO$_3$ oxides via soft chemistry and calcined the final materials at different temperatures from 500 to 1000 °C. With the aim of obtaining morphological and structural information relevant to their performance the prepared oxides have been thoroughly characterized by BET, Power Neutron Diffraction (PND), XRD, HRTEM, STEM-HAADF and XPS. We have analysed the effect of extrinsic (surface area and particle size) and intrinsic factors (formation of oxygen vacancies, Ni oxidation states and occupancy of the e$_g$ levels) on the current densities and specific activity, respectively, of several samples of LaNiO$_3$. The catalysts with higher catalytic activity are those in which the perovskite structure is properly formed, but display high surface areas.

© 2016 Elsevier B.V. All rights reserved.

1. Introduction

The finding of efficient electrocatalysts based on abundant, well distributed non-critical raw materials is a central issue for the development of the electrochemical technologies involved in the transformation of renewable energy. From the electrocatalyst point of view, both the oxygen reduction reaction (ORR) and oxygen evolution reaction (OER) are the bottleneck processes of fuel cells and batteries. The low kinetics of the ORR ($O_2 + 2H_2O + 4e^- \rightarrow 4OH^-$) is responsible for most of the voltage losses in proton exchange fuel cells (PEMFC) [1,2]. As a consequence, state-of-the-art ORR catalysts are based in noble precious metals, mainly Pt and PtCo alloys. However, Pt resources are limited and unevenly distributed on Earth and, as a result, the price of the electrocatalysts accounts to more than 30% of the total PEMFC cost [3,4]. Therefore, current investigations are mainly focused on finding ORR electrocatalysts based on abundant and inexpensive materials. Among those, transition metals coordinated to N atoms in a C—C matrix (akin to the heme group) [5] and transition metal oxides are the most promis-

ing approaches [6,7]. The first perovskite oxides probed as catalysts for the ORR were reported in the 80′s by Bockris and Otagawa [8]. They already predicted that the catalytic activity of these materials was related to the number of *d* electrons of the transition metals of the perovskite, which are the catalytic active atoms on the perovskite, and to the strength of the metal-OH bond. The best-known oxide catalysts for the ORR are manganese and nickel based perovskites [9]. These oxides are very promising, not only because they present high activities in the ORR and OER but also because of their relative high conductivity ($\sim$0.05 Ω^{-1} cm^{-1} for LaMnO$_3$ and $\sim$1000 Ω^{-1} cm^{-1} LaNiO$_3$) and their low cost [10,11]. LaNiO$_3$ presents one of the highest ORR activity reported for this kind of materials. The first work about the electrocatalytic activity of the LaNiO$_3$ family was published in 1978, showing that the compound was a promising catalyst [12]. LaNiO$_3$ is a simple perovskite that crystallizes in a rhombohedral structure. The general perovskite structure (ABO$_3$) is one of the most extended structures for complex oxides. It can accommodate a huge variety of cations in both A and B sublattices. B cations are situated on octahedral sites, while A cations are in the voids in between these octahedra in larger cages usually with dodecahedral coordination. However, depending on the sizes of A and B cations, the structure can be distorted and A cations can present lower coordination. Thus, A sites can accom-

* Corresponding authors.
E-mail addresses: m.retuerto@csic.es (M. Retuerto), srojas@icp.csic.es (S. Rojas).

modate many different cations with different sizes (mainly alkaline and rare earths) and B sites also have the versatility to host different cations with variable oxidation states, generally transition metals [13–15].

Although these oxides are promising candidates for both the ORR and OER, several drawbacks inherent to the synthesis and nature of these oxides have to be addressed. For instance, in order to obtain oxides with the perovskite structure, high temperature treatments are employed producing oxides with very large crystal sizes and as a consequence low specific surface areas (of the order of $2–10\,m^2\,g^{-1}$) resulting in low catalytic activities. In principle, in order to increase the catalytic activity of perovskites efforts should be directed to increase the specific surface area of the oxides. One possible strategy is the use of ball-milling, but it has been reported that this method does not produce a sufficient miniaturization of the particle size of the oxides [16]. Another inconvenient found on these materials is that they tend to agglomerate during the synthesis, which has a detrimental effect in the catalytic activity.

Recently, a great deal of research has been conducted in order to improve the catalytic performance of $LaNiO_3$ for the ORR. This is because $LaNiO_3$ is one of the most active mixed-oxide catalysts for the ORR, with an specific activity of 0.908(8)V (versus RHE) at $25\,\mu A/cm^2_{oxide}$, a value comparable or even higher than that of similar perovskites such as $LaMnO_{3+\delta}$ with ~0.91 V or $LaCoO_3$ with 0.847(3) V [8]. For instance, Sakthivel et al. [17] studied the effect of mixing different carbons to $LaNiO_3$ ink; Zhou et al. [18] investigated the effect of the possible different crystal structures of the oxide; Hardin et al. [19] studied $LaNiO_3$ nanoparticles supported on nitrogen-doped carbons; Petrie et al. [20] reported particle strain-catalytic activity relationships. More recently, Shao-Horn's group has investigated thoroughly the parameters that potentially govern the binding strength of the intermediates at the perovskite surface, in order to rationalize ORR activity and thus predicting new oxide catalysts [9]: i) they have developed the theory of the near-unity occupancy of the e_g orbital of the d states of the transition metals of the perovskites [7]; ii) they have studied the consequences of the hybridization between the d states of the transition metals and the $2p$ states of the oxygen ions [21]; iii) the influence of the pH [22]; iv) the impact of the catalytic process on the surface of the oxides [23] and the effects that are produced on the structure and oxidation states [24]; v) the influence of different morphologies, for instance, measuring oxides as thin films [25]; vi) they have also studied carefully the methodology of the measurements observing that $LaNiO_3$ is stable only within a narrow potential window. The lack of stability over a wide potential range is in fact among the most serious concerns for the use of $LaNiO_3$ (and in general of most perovskites and complex oxides) as electrocatalysts [6].

Despite of the important body of work described above, several key factors governing the electrocatalytic performance of $LaNiO_3$ (or other perovskites) for the ORR, such as the effect of particle size, have not been addressed hitherto. The effect of the particle size on the ORR catalytic activity has been studied for other similar oxides [26,27]. In this work we report a systematic study of the effect of the crystal size of $LaNiO_3$ for the ORR. In addition, a detailed determination of the crystal structures and oxygen quantities of the samples has been conducted by using Neutron Powder Diffraction (PND).

2. Experimental section

2.1. Synthesis of LaNiO₃

$LaNiO_3$ perovskite oxides were synthesized in polycrystalline form by a soft-chemistry procedure in order to obtain very reactive precursors and thus reduce the final synthesis temperature. Stoi-chiometric amounts of La_2O_3 (Sigma Aldrich 99.99% trace metals basis, heated at $1000\,°C$ in air before we used it to ensure the stoichiometry of the final compound) and NiO (Sigma Aldrich 99.99% trace metals basis, used as received) were dissolved in a 0.1 M solution of citric acid (Sigma Aldrich assay ≥99.5%) (150 mL). In order to ensure the complete dissolution of the oxides, 20 mL of nitric acid (Panreac 65%) was added to the mixture. The mixture was stirred at ~150 °C until complete evaporation. This procedure led to the formation of resins containing a homogeneous distribution of the metal cations, which were dried afterwards at 450 °C for 12 h, allowing the elimination of the organic material and nitrates. Finally, the samples were subjected to heat-treatments at the desired temperatures for the study of 500, 600, 700, 800, 900 or 1000 °C under O_2 flow. $LaNiO_3$ perovskites were synthetized under an O_2 flow in order to avoid the formation of competing phases as the Ruddlesden–Popper $La_{n+1}Ni_nO_{3n+1}$ (n = 1,2 and 3) oxides. The materials obtained were labelled as T-$LaNiO_3$ where the prefix T indicates the temperature of the thermal treatment.

2.2. Physicochemical characterization

Textural properties were evaluated by N_2 adsorption–desorption isotherms of the samples recorded at liquid N_2 temperature with a Micromeritics ASAP 2000 apparatus. Samples were degassed at 140 °C under vacuum for 24 h. Specific areas were calculated by applying the Brunauer–Emmett–Teller (BET) method within the relative pressure range P/P_0 = 0.05–0.30.

X-ray Powder Diffraction (XRD) in Bragg-Brentano reflection geometry with CuK_α radiation (λ = 1.5418 Å) was used to determine the phases and its purity. In situ variable temperature XRD (between 400 °C and 800 °C) was also performed to determine the evolution of the oxides obtained with temperature and to identify the temperature where the perovskite phase is actually formed and compare the width of the reflections at several temperatures for crystalline domain size determination.

Powder Neutron Diffraction (PND) characterization was carried out in the high-resolution powder diffractometer D2 B located at ILL, Grenoble, France. It was collected at room temperature and λ = 1.594 Å. Three representative samples namely 700-$LaNiO_3$, 800-$LaNiO_3$ and 900-$LaNiO_3$ were studied for comparison. For the refinement of the crystal structures of the samples we used the Rietveld method and the Fullprof crystallographic program [28,29]. The function selected to generate the diffraction peaks shape was pseudo-Voigt. The parameters refined in the final run were the scale factor, background coefficients, zero-point error, pseudo-Voigt corrected for asymmetry parameters, positional coordinates, isotropic thermal factors an occupancy factors for oxygen atoms.

Transmission Electron Microscopy (TEM) data, Energy Dispersive X-ray spectra (EDX) and Scanning Transmission Electron Microscopy-High Angle Annular Dark Field (STEM-HAADF) data, were recorded on a JEOL 2100 field emission gun transmission electron microscope operating at 200 kV and equipped with an EDS spectrometer Oxford INCA Energy 2000 system. Specimens were prepared by depositing small portions of the samples to be investigated onto a Cu grid supporting a lacey carbon film. Deposition was achieved by preparing a suspension of the material in ethanol.

X-ray photoelectron spectra (XPS) were acquired with a VG ESCALAB 200 R at a pass energy of 50 eV using a Mg Kα X-ray source. The kinetic energies of the photoelectrons were measured using a hemispherical electron analyser working in the constant-pass energy mode. The background pressure in the analysis chamber was kept below 3×10^{-8} mbar during data acquisition. At least 200 scans were collected in increments of 0.1 eV with dwell times of 50 ms in order to increase the signal-to-noise ratio Binding energies (±0.2 eV) were determined by setting the C 1 s peak at 284.8 eV.

2.2.1. Electrochemical characterization

The electrochemical performance of the T-LaNiO$_3$ samples was tested in a computer controlled Autolab PGstat 302N potentiostat/galvanostat. A standard three-compartment glass cell and a rotating disk electrode (RDE) (Pine Rresearch Intruments) were used. An Au rod and a homemade Reversible Hydrogen Electrode (RHE) were used as counter and reference electrodes, respectively.

For the measurement of the electrocatalytic performance a protocol similar to that reported by Gasteiger et al. and Shao Horn et al. has been followed [6,7,9]. The T-LaNiO$_3$ samples were deposited on the electrode by means of an ink, mixing fine powders of the catalyst under study with carbon black (Vulcan-XC-72R) at a 5:1 mass ratio, respectively. The oxide is mixed with a high surface area carbon, as Vulcan, to eliminate issues related to electronic conductivity. Tetrahydrofuran (THF) and Nafion (2:1 mixed with 0.1 M NaOH solution) were added to the oxide-carbon black mix, yielding inks with a constant final concentration of 5 mg$_{oxide}$ mL^{-1}$_{ink}$, 1 mg$_{carbon}$ mL^{-1} $_{ink}$, 0.03 mL$_{Nafion}$ mL^{-1} $_{ink}$, 0.97 mL$_{THF}$ mL^{-1} $_{ink}$. After sonication with an Ultrasonic Processor UP50H (Hielscher), 20 µL of the catalyst ink was dispersed onto a GC electrode (0.196 cm^2 area), leading to a loading of 0.1 mg of catalyst on the electrode.

First, a series of cyclic voltammograms were recorded from 0.6 V to 1.1 V at a scanning rate of 50 mV s^{-1} in Ar purged 0.1 M KOH electrolyte until a stable response was obtained. Next, three voltammograms were recorded at 10 mV s^{-1} under the same experimental conditions. For the measurement of the ORR activity, the electrolyte was saturated in O$_2$ and polarization curves were recorded at 1600 rpm from 0.6 to 1.1 V at 10 mV s^{-1}. Faradaic ORR currents (i$_f$) curves were capacitance-corrected by subtracting the curves obtained in the Ar saturated electrolyte. iR-correction was done by calculating the ohmic resistance obtained from Electrical Impedance Spectroscopy (EIS) at open voltage. Faradaic current densities (j$_f$) were calculated by normalizing the faradic current (i$_f$) to the geometric area of the electrode (j$_f$ in mAcm^{-2}$_{geo}$). Specific activities (i$_s$ in µAcm^{-2}$_{oxide}$) were calculated by normalizing i$_f$ to the actual specific surface area of the oxide deposited on the electrode using the following equation:

$$i_s = \frac{i_f}{(g_{oxide} x BET_{oxide})} \qquad (1)$$

where BET$_{oxide}$ is the specific surface area of the oxide obtained from the BET method.

The ORR can proceed via 4 or 2 electrons pathway, producing H$_2$O or H$_2$O$_2$, respectively. The production of H$_2$O$_2$ was evaluated during the measurement of the ORR with a RRDE with a Pt ring set at 1.2 V, as reported elsewhere [30]. The amount of H$_2$O$_2$ produced was estimated with the following equation:
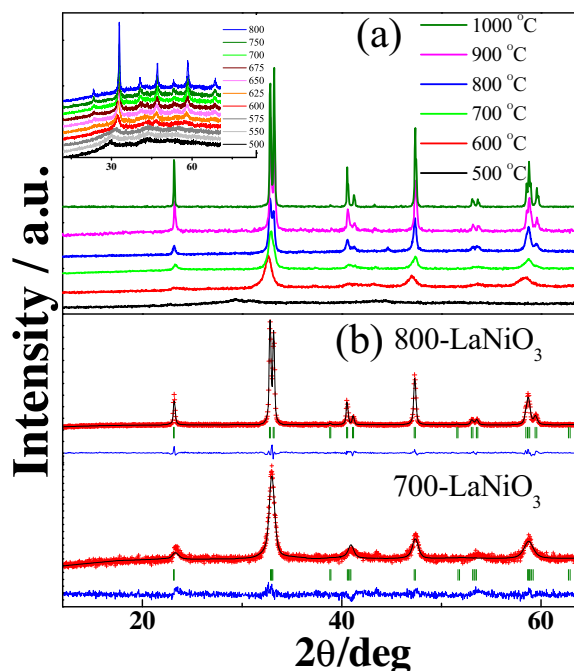
$$\%HO_2^- = \frac{2I_{R/N}}{I_D + I_{R/N}} \times 100 \qquad (2)$$

where I$_R$ and I$_D$ are the currents recorded in the ring and in the disk, respectively and N is the collection efficiency (26%).

3. Results and discussion

3.1. Sample characterization

Fig. 1a shows the room temperature XRD patterns of the samples prepared at 500, 600, 700, 800, 900 and 1000 °C. The diffraction lines of LaNiO$_3$ perovskite phase are observed for the samples synthesized at 600 °C and above. On the other hand, the lack of reflections in the diffractogram for 500-LaNiO$_3$ indicates that the perovskite is not formed at such low temperature.

Fig. 1. (a) Room temperature XRD patterns for LaNiO$_3$ prepared at 500, 600, 700, 800, 900 and 1000 °C. Inset: *in situ* variable temperature XRD patterns of LaNiO$_3$ in air between 500 °C and 800 °C. (b) Rietveld refinements of the structure of LaNiO$_3$ from XRD of the samples prepared at 700 °C (b) and 800 °C; Observed (red crosses), calculated (black full line) and difference (bottom blue line) profiles. Green lines are the Bragg reflections. (For interpretation of the references to colour in this figure legend, the reader is referred to the web version of this article.)
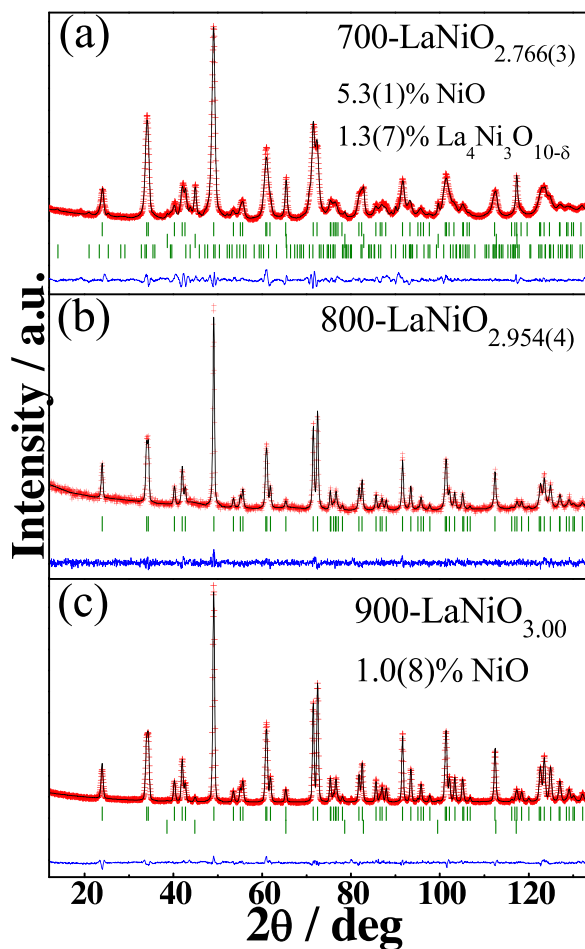
Table 1
Cell parameters for T-LaNiO$_3$ as refined from XRD[*].

Sample	a/Å	c/Å	V/Å^3
600-LaNiO$_3$	5.415(3)	13.078(13)	332.1(4)
700-LaNiO$_3$	5.448(4)	13.253(8)	340.7(4)
800-LaNiO$_3$	5.4635(7)	13.171(2)	340.50(8)
900-LaNiO$_3$	5.4584(7)	13.149(2)	339.29(8)
1000-LaNiO$_3$	5.458(1)	13.150(2)	339.29(10)

[*] Values in parentheses are the errors of the refinements.

As observed in Fig. 1a, the diffraction lines become better resolved (more intense and smaller breaths) with the increasing temperature of the thermal treatment. This behavior indicates that the crystallinity of the samples increases with the increasing temperature of the thermal treatment, *i.e.*, the size of the crystalline domains increases with temperature. The inset to Fig. 1a shows the XRD patterns for LaNiO$_3$ collected *in-situ* at increasing temperatures between 500 °C and 800 °C in air. The perovskite is formed between 600 and 650 °C in agreement with the synthesis temperatures.

Our XRD data show that the LaNiO$_3$ samples obtained in this work crystallize in a rhombohedral symmetry with space group R-**3**. The structures of the T-LaNiO$_3$ samples synthesized at T > 600 °C were all refined using this space group, and no other symmetries were considered. These results are different from that reported by Zhou *et al.* [18] who reported cubic LaNiO$_3$ structures for similar samples prepared at the same temperatures. This discrepancy could be related to the very rapid quenching of the LaNiO$_3$ samples prepared by Zhou's group and/or the different atmosphere used for the synthesis. The cell parameters obtained from the refinement of the XRD crystal structure of all samples (see Fig. 1b) are listed in Table 1. The parameters obtained are consistent with LaNiO$_3$ phase.

Fig. 2. Rietveld refinements of the structure of LaNiO₃ by PND of the samples prepared at (a) 700 °C, (b) 800 °C and (b) 900 °C. Red crosses are the experimental neutron data, black line are the calculated diffractograms and the blue line is the difference, green lines are the Bragg reflections for LaNiO₃ (upper), NiO (middle) and La₄Ni₃O₁₀₋δ (bottom) phases. (For interpretation of the references to colour in this figure legend, the reader is referred to the web version of this article.)

Table 2
Cell parameters, atom occupancies and selected interatomic distances and discrepancy factors for LaNiO₃ refined from PND at 295 K in the R-3c space group.

	700-LaNiO₃	800-LaNiO₃	900-LaNiO₃
a/Å	5.4562(2)	5.45666(16)	5.45727(6)
c/Å	13.1584(8)	13.1373(5)	13.1347(2)
V/Å³	339.25(3)	338.759(19)	338.767(7)
La 6a(0 0 ¼)			
B_{iso}/Å²	0.33(3)	0.35(6)	0.25(2)
Ni 6b(0 0 0)			
B_{iso}/Å²	0.63(3)	0.11(5)	0.16(2)
O1 18e(x 0 ¼)			
x	0.4563(2)	0.4549(3)	0.45409(12)
B_{iso}/Å²	0.07(3)	0.49(8)	0.57(2)
Occupancy O1	0.922(3)	0.984(4)	1.000
% NiO	5.3(1)	0	1.0(8)
% La₄Ni₃O₁₀₋δ	1.3(7)	0	0
LaO₁₂ Polyhedra			
La-O1 (x 3)	2.4897(6)	2.4822(11)	2.4902(12)
La-O1 (x 3)	2.9665(6)	2.9744(11)	2.9671(12)
La-O1 (x 6)	2.7106(6)	2.7085(12)	2.7076(6)
<La-O>	2.7193(2)	2.7184(11)	2.8210(2)
NiO₆ Octahedra			
Ni −O1 (x 6)	1.9339(2)	1.9340(17)	1.9331(9)
χ^2	18.4	1.37	4.21
R_p/%	4.63	4.61	3.40
R_{wp}/%	6.51	3.66	2.61

A more accurate determination of the crystal structure, impurities, differences between samples and oxygen vacancies is attained from PND. Neutron Diffraction is a very powerful technique to study oxides since the coherent scattering length of oxygen is very large as compared to its X-ray scattering factor. Fig. 2 shows the PND for 700-LaNiO₃, 800-LaNiO₃ and 900-LaNiO₃ samples along with the refinement of their crystal structures. In the three cases LaNiO₃ is defined in the rhombohedral space group with similar cell parameters. The large size of La³⁺ cation for the A site of the perovskite determines its slightly distorted rhombohedral structure (R-**3c**), which is also the responsible of its metallic character and the absence of metal-insulator transitions, unlike other RNiO₃ with different structure, for instance, RNiO₃ (R = Pr, Nd, Sm and Eu) that present metallic-insulator transitions at 130 K, 200 K, 400 K and 460 K, respectively [31]. The metallic behavior of LaNiO₃ is an advantage to be used as electrocatalysts. Table 2 includes the final atomic coordinates, occupancies, impurities, atomic distances and discrepancy factors after refinement.

PND was fundamental from a structural point of view, in order to determine the differences in the crystal structure, impurities and content of oxygen of the samples. This technique allows us to evaluate the oxygen content, which is directly related to nickel oxidation state, and thus to the e_g occupancy of Ni active site of the perovskite. All these parameters are expected to have a deep impact on the catalytic performance of the T-LaNiO₃ samples. The major differences found by PND between the samples are: i) 700-LaNiO₃ has much broader peaks than the other two samples indicating smaller particle size (in good agreement with XRD data); ii) the content of oxygen of 700-LaNiO₂.₇₇(₂) is lower than that of 800-LaNiO₃ and 900-LaNiO₃, which are close to the stoichiometric values; iii) 700-LaNiO₃ presents the following impurities: 5.3(1)% of NiO and 1.3(7)% of La₄Ni₃O₁₀₋δ, while 800-LaNiO₃ is pure and 900-LaNiO₃ only contains 1.0(8)% of NiO. These impurities are not observed by XRD. The larger quantity of impurities in 700-LaNiO₃ indicates that this temperature is still below the optimum temperature to form a pure and stoichiometric perovskite. The possible effect of these impurities and the different content of oxygen on the catalytic activity of LaNiO₃ will be considered.
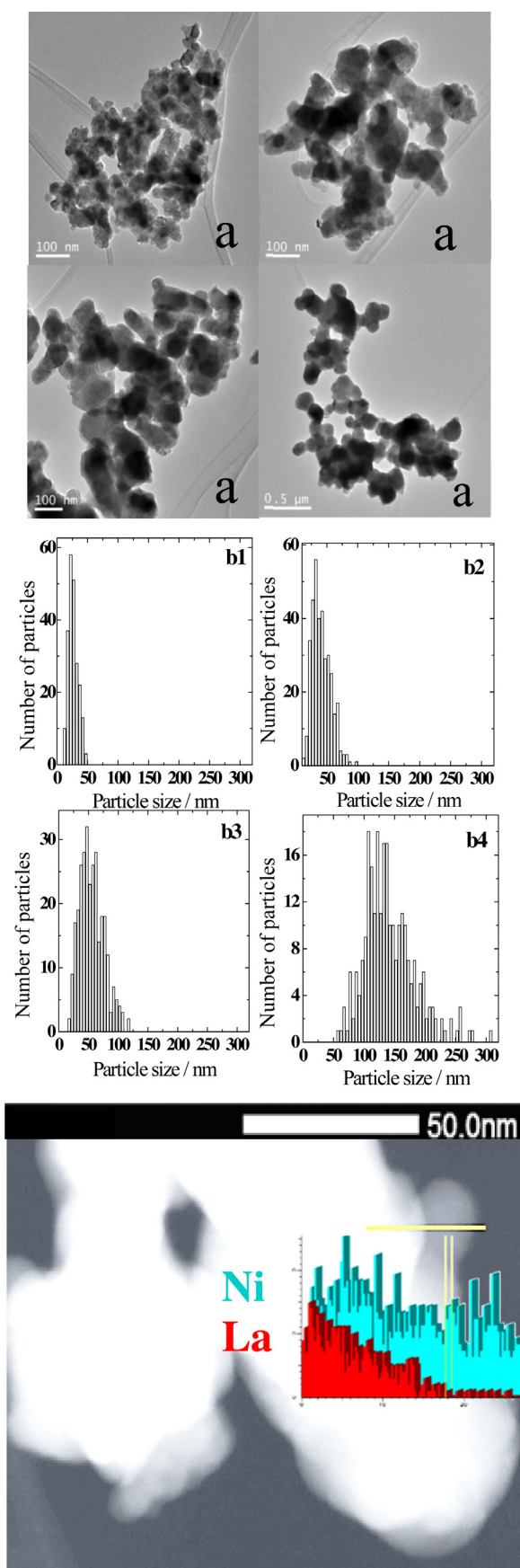
In order to get accurate size-activity relationship, it is imperative to identify accurately the crystal size of the T-LaNiO₃ samples. Thus, different methods to calculate the crystal size of the LaNiO₃ perovskites were used. In a first approach, the crystallite size was obtained from the Scherrer equation assessed with the data obtained from the X-ray diffraction patterns:

$$D = \frac{k\lambda}{\beta_{size}\cos\ \theta} \quad (3)$$

where k is the Scherrer constant ($k \approx 0.9$), λ is the incident wavelength, Θ is the diffraction angle. β_{size} can be the experimental full-width at half-maximum (FWHM) or the experimental Integral Breadth (ratio of the peak area vs peak maximum). We used the FWHM for β_{size} in our calculations. This equation is usually employed to obtain an estimated value of the size of the X-ray coherent diffracted crystalline domains (D). However, this method for determining grain size neglects contributions from lattice strain. In order to account for strain effects, we also used the Williamson-Hall relationship which is an extended version of the Scherrer equation considering that the strain effect has a different variation than the size effect with respect to the Bragg angle [32,33]:

$$\beta_{total} = \beta_{size} + \beta_{strain} = \frac{k\lambda}{D\cos\theta} + 4\eta\frac{\sin\theta}{\cos\theta} \quad (4)$$

$$\beta_{total}\cos\theta = \frac{k\lambda}{D} + 4\eta\sin\theta \quad (5)$$

In this case β_{total} is FWHM and $\eta = \Delta d/d$ is the strain parameter (Δd is the difference of the lattice d spacing). We represent a linear fit where $y = \beta_{total}\cos\theta$ and $x = 4\sin\theta$; from the intersection with y we obtain the crystal size and from the slope we obtain the strain.

The methods above give an average value of the crystalline domain size of the grains; however, real samples usually comprise grains with different domains. In order to evaluate the distribution of sizes of the grains, and to account for the non-coherent domains, TEM images were recorded. Fig. 3a shows representative TEM images for the LaNiO$_3$ powders prepared at 600, 700, 800 and 900 °C, which show that the particles tend to agglomerate with the increasing synthesis temperature. The histograms presented in Fig. 3b show the particle size distributions obtained by counting at least 200 particles in the TEM images. Assuming LaNiO$_3$ particles as spheres and measuring only the ones which are sufficiently isolated we can represent the diameter *vs.* the number of particles for all LaNiO$_3$ samples. The resulting particle distributions are well fitted to a Gaussian function. From the fit we obtain the mean value and the standard deviation of each sample, which are outlined in Table 3. As expected, TEM results show a clear increment of particle size with the increasing calcination temperature. Sample 600-LaNiO$_3$ shows a narrow distribution of sizes with an average value of 24(6) nm. The average values for samples 700-LaNiO$_3$ and 800-LaNiO$_3$ shift to 37(14) and 51(20) nm, respectively. 900-LaNiO$_3$ and 1000-LaNiO$_3$ show larger particles with average values of 132(32) and 250(40) nm, respectively. Fig. 3c depicts a representative STEM-HAADF micrograph of 600-LaNiO$_3$ together with an EDX line scan, showing a profile composition along two crystals. The first region, which corresponds to the main perovskite phase, displays the characteristic EDX profiles of La and Ni. The second one only presents peaks for Ni, suggesting the presence of small particles of NiO and/or Ni carbonate at the surface of 600-LaNiO$_3$. PND and TEM results indicate that below 800 °C the perovskite is still in the process of being formed with presence of small impurities that eventually disappear when the temperature rises. The LaNiO$_3$ perovskite is completely formed and pure already at 800 °C; above 800 °C the effect of the temperature is mainly to improve the crystallinity and thus to increase the crystal size.

Table 3 collates particle sizes for LaNiO$_3$ samples obtained by the different analytical techniques. Grain sizes obtained by TEM for sample 600-LaNiO$_3$ and 700-LaNiO$_3$ are around 20–35 nm, increasing to ~50 nm for sample 800-LaNiO$_3$, and larger than 100 nm for 900-LaNiO$_3$ and 1000-LaNiO$_3$. It is worth noting that the average particle sizes obtained by TEM fairly coincide with the crystallite size values deduced from the XRD-Scherrer and Williamson-Hall equation for samples 600-, 700- and 800-LaNiO$_3$. By contrary, both analyses give quite different results for sample 900- and 1000-LaNiO$_3$, because for particles bigger than 100 nm the Scherrer and Williamson-Hall equations are out of the equipment limitations.

The electrochemically active surface area (ECSA) in m^2 g$^{-1}_{oxide}$ calculated from the double-layer capacitance and the mass surface area (dispersion) calculated from the volume/surface diameter ($d_{v/s}$) of the particles are also shown for comparison. Details for the calculation of the ECSA and dispersion are given in the Supplementary information.

3.2. Surface composition

The nature and surface composition of all LaNiO$_3$ samples was studied by XPS (Table 4). The Ni 2p core-level presents a single doublet with Ni 2$p_{3/2}$ core-levels at 855.4 eV characteristic of Ni^{2+}/Ni^{3+}

Fig. 3. (a) TEM images of LaNiO$_3$ samples as a function of calcination temperature: 600 (a1), 700 (a2), 800 (a3), 900 °C (a4); (b) Particle size distribution for 600 (b1), 700 (b2), 800 (b3), 900 °C (b4). (c) 600-LaNiO$_3$ STEM-HAADF micrograph and EDX line scan showing the profile composition along two crystals. The first region displays the EDX profile of La and Ni but the second one only Ni, indicating that the small particles in the surface do not have La.

Table 3
Particle sizes and specific surface areas for LaNiO$_3$ samples.

Sample	Coherent Domain Size- from Scherrer Eq. /nm	Coherent Domain Size- from Williamson-Hall Eq. /nm	Grain Size (d)- from TEM /nm	Volume/area average diameter (d_{va}) /nm	Mass surface area (A_S)[**] /m^{2}g^{-1}	BET-surface area /m^{2}g^{-1}	ECSA[**] /cm^2
600-LaNiO$_3$	20(8)	12(2)	24(6)	35	24	13	64
700-LaNiO$_3$	35(8)	26(3)	37(14)	49	17	7	13
800-LaNiO$_3$	50(8)	33(6)	51(20)	68	12	4	9
900-LaNiO$_3$	72(10)[*]	58(4)[*]	132(32)	149	6	3	4
1000-LaNiO$_3$	83(10)[*]	71(4)[*]	250(40)	252	3	2	3

[*] When the crystal size is larger than 100 nm the Scherrer equation is out of range and the results cannot be taken into account.
[**] *Mass surface area* (calculated from $d_{v/s}$) and *ECSA* (calculated from the double-layer capacitance), see SI for details.

Table 4
Binding energies and Ni Auger line (eV) of T-LaNiO$_3$ samples.

Sample	Binding Energy/eV				Ni$_{sat}$/Ni 2p$_{3/2}$
	La 3d$_{5/2}$	Ni 2p$_{3/2}$	O 1s[*]	C 1s	
700-LaNi	834.5	855.4	528.6 (35) 531.2 (65)	289.3	0.527
800-LaNi	834.6	855.8	528.9 (31) 531.4 (69)	289.5	0.532
900-LaNi	834.5	855.7	528.8 (43) 531.2 (57)	289.4	0.383

[*] Values in parentheses show the relative atomic concentration of each species.

species. The presence of satellite peaks at the high binding energy region of the principal peak indicates the presence of Ni^{2+} species. XPS data fail to provide an accurate estimation of the fraction of Ni^{2+}/Ni^{3+} species in the samples. However, the evolution of the relative abundance of these species with the calcination temperature can be derived from the evolution of the ratio between Ni satellite and Ni 2$p_{3/2}$ peaks for each sample. As shown in Table 4, the Ni$_{sat}$/Ni 2$p_{3/2}$ ratio decreases in the order 700-LaNiO$_3$ ∼ 800-LaNiO$_3$ > 900-LaNiO$_3$ indicating that the fraction of surface Ni^{2+} species decreases with the increasing temperature of synthesis of the samples. This observation is in agreement with Ni 2p core level which presents a slight lower BE for 700-LaNiO$_3$. This reduction could be related to less Ni^{2+} impurities or less oxygen vacancies in the perovskite when the temperature increases. La 3d core-level region appears as a doublet of doublets (due to the shake-up process O 2p → La 4f) with the La 3$d_{5/2}$ peak at 834.5 eV ascribed to La^{3+} species. The O 1s core-level spectra of the samples have two peaks at ca. 528.6 and 531.2 eV ascribed to lattice oxygen (O^{2-}) and chemisorbed oxygen species (OH$_{ads}$, carbonates...), respectively [34]. The C 1s spectra show a small contribution from spurious carbon species at ca. 284.6 eV and a peak at ca. 289.4 eV indicative of the presence of surface carbonates. Unfortunately, it is not possible to discriminate whether this peak accounts for La or Ni carbonates. However, based upon the STEM results discussed above, we ascribed this peak to the presence of surface Ni carbonates.

3.3. Electrochemical performance

The electrocatalytic performance of LaNiO$_3$ samples for the ORR has been evaluated in oxygen saturated 0.1 M KOH electrolytes between 0.6 and 1.1 V at 10 mVs^{-1} with a RDE at 1600 rpm. Potentials less positive than 0.6 V were not considered because the perovskite is not stable at potentials below ∼0.4–0.5 V. The Pourbaix diagrams for Ni oxides [35] show that, at pH = 13, Ni^{3+} species are reduced into Ni^{2+} species. In our samples, Ni is in 3+ oxidation state and decreasing the potential below 0.4–0.5 V would move Ni^{3+} into Ni^{2+}, resulting in a final collapse of the LaNiO$_3$ perovskite structure. As a consequence, the diffusion limiting region for reduction of O$_2$ is not reached.

Fig. 4a shows the current densities (j_f in mA/cm$^2_{geom}$) obtained for all T-LaNiO$_3$ perovskites. The onset potentials, (E$_{onset}$) defined as the potential at which j_f = −0.1 mAcm$^{-2}_{geom}$, are used for comparison purposes. Catalysts 700-LaNiO$_3$ and 800-LaNiO$_3$ show the most positive E$_{onset}$ in the series of ∼0.93 V, followed by 600-LaNiO$_3$ with E$_{onset}$ at 0.91 V. These values are in line with the previously reported value below ∼0.95 V for LaNiO$_3$, and it is significantly more positive than that reported for other perovskites such as LaCu$_{0.5}$Mn$_{0.5}$O$_3$ of ca. 0.8 V [6]. This onset potential is lower than that reported for Fe/N/G of 1.04 V [30] but more positive than that reported for Co/graphene catalysts of 0.97 V (at −0.15 mAcm^{-2}) [36]. The catalysts obtained at the highest (900- and 1000-LaNiO$_3$) and lowest (500-LaNiO$_3$) calcination temperatures have the less positive E$_{onset}$ potentials in the series (0.86 V for 900-LaNiO$_3$, 0.82 V for 1000-LaNiO$_3$ and 0.68 V for 500-LaNiO$_3$).

800-LaNiO$_3$ and 700-LaNiO$_3$ show the highest current densities of the series in the whole range of potentials studied. However, as observed in Fig. 4a, 800-LaNiO$_3$ has higher current density than 700-LaNiO$_3$ at E < 0.85 V. Finally, 500-LaNiO$_3$ is not active for the ORR, and the activity measured with this sample is the same as that measured with the bare glassy carbon electrode (Fig. 4a). This is probably because the perovskite is still not formed at this low temperature. This observation confirms that the perovskite structure is the responsible for the ORR activity of the samples.

The ORR can proceed via 4 or 2 electrons pathway, producing H$_2$O or H$_2$O$_2$, respectively. The production of H$_2$O$_2$ was evaluated during the measurement of the ORR with a RRDE with a Pt ring set at 1.2 V. The production of H$_2$O$_2$ is insignificant (below 1%) in all cases, indicating that the formation of H$_2$O, *i.e.*, the 4 electrons is the preferred reaction pathway. Admittedly, this apparent low H$_2$O$_2$ production should be taken carefully since it has been reported that the accurate determination of the H$_2$O$_2$ production should be conducted by studying electrodes with different thicknesses [37].

The lower ORR activity of samples 900-LaNiO$_3$ and 1000-LaNiO$_3$ for the ORR (as compared to the catalysts prepared at 800 and 700 °C) probably accounts to the larger size of the LaNiO$_3$ particles and, consequently, to the lower BET areas of the oxides prepared at high temperatures.

In order to extract the effect of the surface area, Fig. 4b represents the specific activities (i_s in μA/cm$^2_{oxide}$) calculated by
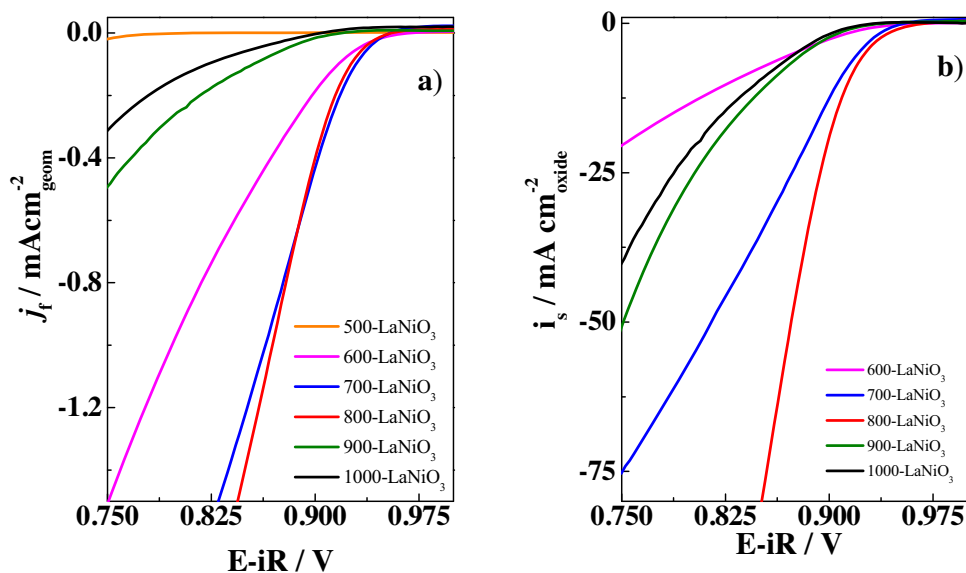
Fig. 4. (a) Current density and (b) Specific activity curves for LaNiO$_3$ samples in O$_2$ saturated 0.1 M KOH at 1 mVs^{-1} and 1600 rpm.

normalizing the ORR activity to the actual area of oxide on the electrode obtained from the N$_2$ adsorption/desorption isotherms. In this work we report the specific ORR activity by normalizing the ORR activity to the actual surface specific area (obtained from the N$_2$ adsorption-desorption isotherms) of oxide deposited on the working electrode.

For the sake of comparison, the ORR activity has been also normalized to the ECSA and to the mass surface area values of the oxides. Further details are shown in the Supplementary information. Although the value of the ORR specific currents obtained for the T-LaNiO$_3$ perovskites depend on the actual factor used for normalization (see Fig. S1), the same trend is observed irrespective of the normalization used, *i.e.*, 800- and 700-LaNiO$_3$ perovskites are the most active ones in the series, both of them showing similar onset potentials but 800-LaNiO$_3$ showing lower overpotentials at higher currents. This trend is not surprising since as shown in Table 3 BET, ECSA and mass surface area values follow the same trend with particle size.

As observed in Fig. 4b, the differences between the specific activity for the ORR of 800-LaNiO$_3$ and 700-LaNiO$_3$ are more evident when normalized to the area of the oxide. First, both samples show similar onset potentials at ca.0.95 V. This value is ca. 30 mV more positive than that of the other perovskites in the series. 800-LaNiO$_3$ shows the highest specific activity in the series (in the entire polarization range under study) followed by 700-LaNiO$_3$. On the other hand, 900-LaNiO$_3$, 1000-LaNiO$_3$ and 600-LaNiO$_3$, record lower ORR activities in the whole polarization range, although 900-LaNiO$_3$ shows slightly higher specific current densities at E < 0.85 V than the other two catalysts. The specific activity of the T-LaNiO$_3$ catalysts was further compared by identifying the potentials at which specific activities of −25 and −50 μAcm^{-2}$_{oxide}$ (Fig. 5a) were reached. 800-LaNiO$_3$ records the most positive potential of the series of 0.90 V at −25 μAcm^{-2}$_{oxide}$, which is the same than previously reported values for LaNiO$_3$ of 0.908(8) V [7]. Also this sample presents the best kinetics for the ORR in the series, with the smallest differences between the potentials at −25 and −50 μAcm^{-2}$_{oxide}$.

As observed in Fig. 5a, when normalized to the BET area, samples 700- and 800-LaNiO$_3$ record similar ORR specific activity, higher than that of samples 600-, 900- and 1000-LaNiO$_3$. The latter samples show higher (600-LaNiO$_3$) and lower (900- and 1000-LaNiO$_3$) surface specific areas than 700- and 800-LaNiO$_3$ indicating that there are parameters swaying the ORR activity other than surface
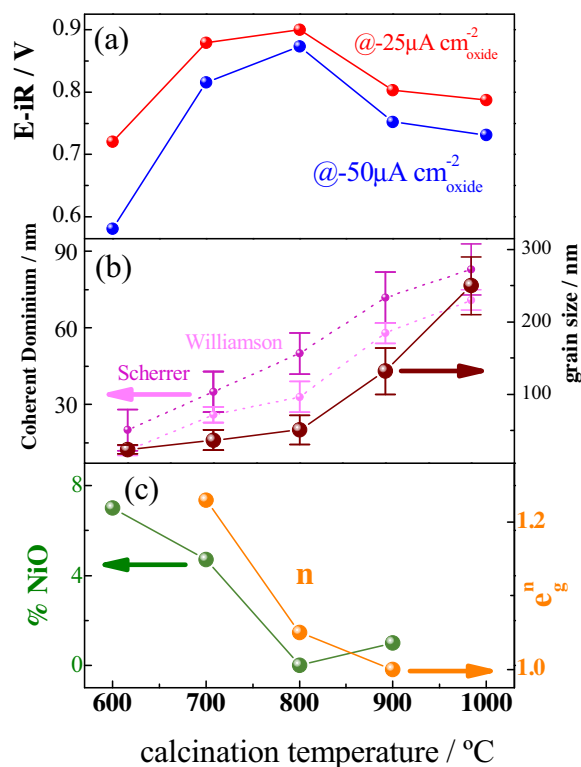

Fig. 5. (a) Potentials to obtain specific activity values of −25 and −50 μAcm^{-2}$_{ox}$, (b) grain size (from TEM) and coherent dominium (by XRD), (c) % NiO impurity and occupation of the antibonding e$_g$ levels.

area and particle size. Several features such as the presence of impurities (phases other than that of the LaNiO$_3$ perovskite) and the presence of oxygen vacancies or the occupancy of the e$_g$ level can influence the catalytic activity of the perovskites.

The presence of impurities has been studied by several techniques including Electron Microscopy and PND. For instance, STEM-HAADF images of 600-LaNiO$_3$ reveal the presence of small impurity grains at the surface of this sample. EDX analyses clearly demonstrate the lack of La atoms on such grains (Fig. 3c), indicating that the surface of the perovskite is enriched in NiO or NiCO$_3$

phases, with a proportion of ∼7%. Thus, and despite the BET area of 600-LaNiO$_3$ is the highest in the series; this sample records a lower ORR activity probably because impurity grains block the access of O$_2$ molecules onto the perovskite active sites. It has been reported that Ni-O phases can be promising oxygen catalysts; however the compounds described with substantial catalytic activities are NiO doped with Fe or Co [38]. In this line, PND reveals the presence of impurities, mostly NiO particles, along with the perovskite phase in 700-LaNiO$_3$ (5% NiO) and in 900-LaNiO$_3$ (1% NiO), see Fig. 5c. However, NiO particles are not observed in 800-LaNiO$_3$, in fact, PND reveals the exclusive formation of the perovskite phase (see Table 2) thus justifying the higher ORR activity of this sample.

Oxygen vacancies have been identified as responsible for the ORR activity of perovskites. The generation of oxygen vacancies in LaNiO$_3$ entails the reduction of a fraction of Ni^{3+} cations in the perovskite into Ni^{2+}. Since Ni^{3+} cations (e$_g^1$) are more active for the ORR than Ni^{2+}, a decreasing in the concentration of the former would result in lower ORR activity. This is clearly observed in Fig. 5 in which the variation of the ORR activity *vs* %NiO and e$_g$ is shown. In this line, the effect of the e$_g^1$ has being studied by Shao-Horn [7] who reported a volcano-like curve for the catalytic activity as a function of the occupancy of the e$_g$ levels of the *d* orbitals of the metal cations in octahedra sites of the perovskite, being the most active ones the oxides with e$_g^1$. Du *et al.* [39] observed the same effect on LaNi$_{1-x}$Mg$_x$O$_3$, in which the activity increases with Mg^{2+}, as the content of Ni^{2+} decreases. It has being also proposed that Ni^{3+} forms oxyhydroxide and hydroxides surface species (*i.e.* NiOOH), which have a strong influence in the faster formation of the intermediates, as HOO* and HO*; producing a faster adsorption and desorption of the oxygen, also due to the higher covalency of the Ni-O bonds, resulting in a higher catalytic activity [39,40]. As shown in Fig. 5c, the optimum e$_g^1$ occupancy is observed in sample 900-LaNiO$_3$ followed by sample 800-LaNiO$_3$. This explains the high activity of the latter sample for the ORR, but fails to explain the low ORR activity observed for sample 900-LaNiO$_3$. As discussed above, the presence of NiO impurities in 900-LaNiO$_3$ has been identified as the cause for its low ORR activity.

In summary, ORR activity of LaNiO$_3$ perovskites is a compromise between several external (BET area, particle size) and intrinsic features (purity of the LaNiO$_3$ phase and occupancy of the e$_g$ levels of the *d* orbitals). Fig. 5 shows that 800-LaNiO$_3$ has the best compromise between these parameters thus recording the best specific activity for the ORR in the series.

The results shown in this work pave the way for the designing of LaNiO$_3$ electrocatalysts with increased ORR activity. Thus, optimized catalysts should contain small LaNiO$_3$ particles in which the perovskite structure is formed completely at low temperature. The challenge is to design optimized synthetic strategies that allow the formation of pure perovskite phases at low temperatures below 600 °C.

4. Conclusions

In this paper we demonstrate the impact of LaNiO$_3$ sample preparation in order to find a good compromise between purity, stoichiometry, oxidation states and crystal size. Also we proved that even if by XRD pure perovskites are observed, PND is a powerful tool to analyze impurities, atomic positions, distances and specially oxygen vacancies and have a clearer idea of the parameters to take into account on the activity of these oxides. From PND and TEM we stablished that below 800 °C the perovskite is not fully developed with impurities and oxygen vacancies that eventually disappear when the temperature rises. Both parameters are detrimental for the catalytic activity of LaNiO$_3$ for the ORR. At 800 °C, the sample is already completely formed and pure, thus resulting in a catalyst

with higher activity. Above 800 °C the effect of the temperature is mainly to increase the size of the crystals, which also hampers the ORR activity.

Appendix A. Supplementary data

Supplementary data associated with this article can be found, in the online version, at http://dx.doi.org/10.1016/j.apcatb.2016.10.016.

References

[1] A. Filpi, M. Boccia, H.A. Gasteiger, Pt-free cathode catalyst performance in H-2/O-2 anion-exchange membrane fuel cells (AMFCs), proton exchange membrane fuel cells 8, pts 1 and 2, electrochemical soc inc, Pennington (2008) 1835–1845.
[2] H.A. Gasteiger, S.S. Kocha, B. Sompalli, F.T. Wagner, Activity benchmarks and requirements for Pt, Pt-alloy, and non-Pt oxygen reduction catalysts for PEMFCs, Appl. Catal. B-Environ. 56 (2005) 9–35.
[3] J. Greeley, I.E.L. Stephens, A.S. Bondarenko, T.P. Johansson, H.A. Hansen, T.F. Jaramillo, J. Rossmeisl, I. Chorkendorff, J.K. Norskov, Alloys of platinum and early transition metals as oxygen reduction electrocatalysts, Nat. Chem. 1 (2009) 552–556.
[4] V.R. Stamenkovic, B. Fowler, B.S. Mun, G.F. Wang, P.N. Ross, C.A. Lucas, N.M. Markovic, Improved oxygen reduction activity on Pt$_3$Ni(111) via increased surface site availability, Science 315 (2007) 493–497.
[5] F. Jaouen, J. Herranz, M. Lefevre, J.P. Dodelet, U.I. Kramm, I. Herrmann, P. Bogdanoff, J. Maruyama, T. Nagaoka, A. Garsuch, J.R. Dahn, T. Olson, S. Pylypenko, P. Atanassov, E.A. Ustinov, Cross-Laboratory experimental study of non-noble-metal electrocatalysts for the oxygen reduction reaction, ACS Appl. Mater. Interfaces 1 (2009) 1623–1639.
[6] J. Suntivich, H.A. Gasteiger, N. Yabuuchi, Y. Shao-Horn, Electrocatalytic measurement methodology of oxide catalysts using a thin-film rotating disk electrode, J. Electrochem. Soc. 157 (2010) B1263.
[7] J. Suntivich, H.A. Gasteiger, N. Yabuuchi, H. Nakanishi, J.B. Goodenough, Y. Shao-Horn, Design principles for oxygen-reduction activity on perovskite oxide catalysts for fuel cells and metal-air batteries, Nat. Chem. 3 (2011) 546–550.
[8] J.O. Bockris, T. Otagawa, Mechanism of oxygen evolution on perovskites, J. Phys. Chem. 87 (1983) 2960–2971.
[9] W.T. Hong, M. Risch, K.A. Stoerzinger, A. Grimaud, J. Suntivich, Y. Shao-Horn, Toward the rational design of non-precious transition metal oxides for oxygen electrocatalysis, Energy Environ. Sci. 8 (2015) 1404–1427.
[10] H.E.H.a.R. Schmidberger, Electronic conductivity in the La(Cr,Ni)O$_3$ perovskite system, J. Electrochem. Soc. 141 (1994) 782–786.
[11] J.J.N.J.A. Souza, R.K. Bollinger, B. McGuire, C.A.M. dos Santos, H. Terashita, Magnetic susceptibility and electrical resistivity of LaMnO$_3$, CaMnO$_3$, and La$_{1-x}$Sr$_x$MnO$_3$ (0.13 ≤ x ≤ 0.45) in the temperature range 300–900 K, Phys. Rev. B 76 (2007) 024407.
[12] Y. Matsumoto, H. Yoneyama, H. Tamura, Mechanism of oxygen reduction at a LaNiO3 electrode, Bull. Chem. Soc. Jpn. 51 (1978) 1927–1930.
[13] A.M. Glazer, Classification of tilted octahedra in perovskites, Acta Crystallogr. Sect. B-Struct. Commun. B 28 (1972) 3384.
[14] P.M. Woodward, Octahedral tilting in perovskites.1. Geometrical considerations, Acta Crystallogr. Sect. B-Struct. Commun. 53 (1997) 32–43.
[15] M.A. Peña, J.L.G. Fierro, Chemical structures and performance of perovskite oxides, Chem. Rev. 101 (2001) 1981–2018.
[16] J. Suntivich, K.J. May, H.A. Gasteiger, J.B. Goodenough, Y. Shao-Horn, A perovskite oxide optimized for oxygen evolution catalysis from molecular orbital principles, Science 334 (2011) 1383–1385.
[17] M. Sakthivel, S. Bhandari, J.F. Drillet, On activity and stability of rhombohedral LaNiO3 catalyst towards ORR and OER in alkaline electrolyte, ECS Electrochem. Lett. 4 (2015) A56–A58.

[18] W. Zhou, J. Sunarso, Enhancing Bi-functional electrocatalytic activity of perovskite by temperature shock: a case study of laNiO3-δ, J. Phys. Chem Lett. 4 (2013) 2982–2988.
[19] W.G. Hardin, D.A. Slanac, X. Wang, S. Dai, K.P. Johnston, K.J. Stevenson, Highly active, nonprecious metal perovskite electrocatalysts for bifunctional metal-Air battery electrodes, J. Phys. Chem Lett. 4 (2013) 1254–1259.
[20] J.R. Petrie, V.R. Cooper, J.W. Freeland, T.L. Meyer, Z. Zhang, D.A. Lutterman, H.N. Lee, Enhanced bifunctional oxygen catalysis in strained LaNiO3 perovskites, J. Am. Chem. Soc. 138 (2016) 2488–2491.
[21] J. Suntivich, W.T. Hong, Y.-L. Lee, J.M. Rondinelli, W. Yang, J.B. Goodenough, B. Dabrowski, J.W. Freeland, Y. Shao-Horn, Estimating hybridization of transition metal and oxygen states in perovskites from OK-edge X-ray absorption spectroscopy, J. Phys. Chem. C 118 (2014) 1856–1863.
[22] L. Giordano, B. Han, M. Risch, W.T. Hong, R.R. Rao, K.A. Stoerzinger, Y. Shao-Horn, pH dependence of OER activity of oxides: current and future perspectives, Catal. Today 262 (2016) 2–10.
[23] K.J. May, C.E. Carlton, K.A. Stoerzinger, M. Risch, J. Suntivich, Y.-L. Lee, A. Grimaud, Y. Shao-Horn, Influence of oxygen evolution during water oxidation on the surface of perovskite oxide catalysts, J. Phys. Chem Lett. 3 (2012) 3264–3270.
[24] M. Risch, A. Grimaud, K.J. May, K.A. Stoerzinger, T.J. Chen, A.N. Mansour, Y. Shao-Horn, Structural changes of cobalt-Based perovskites upon water oxidation investigated by EXAFS, J. Phys. Chem. C 117 (2013) 8628–8635.
[25] K.A. Stoerzinger, M. Risch, J. Suntivich, W.M. Lü, J. Zhou, M.D. Biegalski, H.M. Christen, Ariando, T. Venkatesan, Y. Shao-Horn, Oxygen electrocatalysis on (001)-oriented manganese perovskite films: Mn valency and charge transfer at the nanoscale, Energy Environ. Sci. 6 (2013) 1582.
[26] J. Seo, D. Cha, K. Takanabe, J. Kubota, K. Domen, Particle size dependence on oxygen reduction reaction activity of electrodeposited TaO(x) catalysts in acidic media, Phys. Chem. Chem. Phys. 16 (2014) 895–898.
[27] S. Kéranguéven, Synthesis of efficient Vulcan–LaMnO₃ perovskite nanocomposite for the oxygen reduction reaction, Electrochem. Commun. 50 (2015) 28–31.
[28] H.M. Rietveld, A profile refinement method for nuclear and magnetic structures, J. Appl. Crystallogr. 2 (1969) 65–71.
[29] J. Rodriguez Carvajal, Recent advances in magnetic-structure determination by neutron power diffraction, Physica B 192 (1993) 55–69.
[30] C. Domínguez, F.J. Pérez-Alonso, M.A. Salam, S.A. Al-Thabaiti, M.A. Peña, F.J. García-García, L. Barrio, S. Rojas, Repercussion of the carbon matrix for the activity and stability of Fe/N/C electrocatalysts for the oxygen reduction reaction, Appl. Catal. B: Environ. 183 (2016) 185–196.
[31] J.B. Torrance, P.I. LacorreA. Nazzal, E.J. Ansaldo, Ch. Niedermayer, Systematic study of insulator-metal transitions in perovskites RNiO₃ (R = Pr,Nd,Sm,Eu) due to closing of charge-transfer gap, Phys. Rev. B 45 (1992) 8209–8212.
[32] H. Bi, S.D. Li, Y.C. Zhang, Y.W. Du, Ferromagnetic-like behavior of ultrafine NiO nanocrystallites, J. Magn. Magn. Mater. 277 (2004) 363–367.
[33] L.H. Lewis, A.R. Moodenbaugh, D.O. Welch, V. Panchanathan, Stress, strain and technical magnetic properties of 'exchange-spring' Nd₂Fe₁₄B+α-Fe nanocomposite magnets, J. Phys. D-Appl. Phys. 34 (2001) 744–751.
[34] J.L.G.F.L.G. Tejuca, XPS and TPD Probe Techniques for the study of LaNiO₃ perovskite oxide, Thermochimica Acta 147 (2) (1989) 361–375.
[35] M. Pourbaix, Atlas of Electrochemical Equilibria in Aqueous Solution, 2nd Edition, National Association of Corrosion Engineers, Houston, Texas, USA, 1974.
[36] J. Yu, G. Chen, J. Sunarso, Y. Zhu, R. Ran, Z. Zhu, W. Zhou, Z. Shao, Cobalt oxide and cobalt-Graphitic carbon Core–Shell based catalysts with remarkably high oxygen reduction reaction activity, Adv. Sci. 3 (2016) (1600060-n/a).
[37] A. Bonakdarpour, M. Lefevre, R. Yang, F. Jaouen, T. Dahn, J.-P. Dodelet, J.R. Dahn, Impact of loading in RRDE experiments on Fe–N–C catalysts: two- or four-Electron oxygen reduction? Electrochem. Solid State Lett. 11 (2008) B105–B108.
[38] D. Chen, C. Chen, Z.M. Baiyee, Z. Shao, F. Ciucci, Nonstoichiometric oxides as low-Cost and highly-efficient oxygen Reduction/Evolution catalysts for low-Temperature electrochemical devices, Chem. Rev. 115 (2015) 9869–9921.
[39] Z. Du, P. Yang, L. Wang, Y. Lu, J.B. Goodenough, J. Zhang, D. Zhang, Electrocatalytic performances of LaNi₁₋ₓMgₓO₃ perovskite oxides as bi-functional catalysts for lithium air batteries, J. Power Sources 265 (2014) 91–96.
[40] I.C. Man, H.-Y. Su, F. Calle-Vallejo, H.A. Hansen, J.I. Martínez, N.G. Inoglu, J. Kitchin, T.F. Jaramillo, J.K. Nørskov, J. Rossmeisl, Universality in oxygen evolution electrocatalysis on oxide surfaces, ChemCatChem 3 (2011) 1159–1165.